Available online at www.sciencedirect.com
ScienceDirect
Trans. Nonferrous Met. Soc. China 30(2020) 3016−3030
Transactions of Nonferrous Metals Society of China
www.tnmsc.cn

Effects of heat treatment on microstructure and mechanical properties of Inconel 625 alloy fabricated by wire arc additive manufacturing process

Abolfazl SAFARZADE, Mahmood SHARIFITABAR, Mahdi SHAFIEE AFARANI

Department of Materials Engineering, Faculty of Engineering, University of Sistan and Baluchestan, P. O. Box 98135-674, Zahedan, Iran

Received 12 January 2020; accepted 14 September 2020

Abstract: The microstructure and mechanical properties of Inconel 625 alloy fabricated by wire arc additive manufacturing process were evaluated under as-prepared and heat-treated conditions. A dendritic Ni-based solid solution phase along with (Nb,Ti)C carbide, Laves, and δ-Ni_3Nb secondary phases were developed in the microstructure of the as-prepared alloy. Solution heat treatment led to the dissolution of Laves and Ni_3Nb phases. In addition, dendrites were replaced with large columnar grains. Aging heat treatment resulted in the formation of grain boundary $M_{23}C_6$ carbide and nanometric γ'' precipitates. Hardness, yield and tensile strengths, as well as elongation of the as-prepared part, were close to those of the cast alloy and its fracture occurred in a transgranular ductile mode. Solution heat treatment improved hardness and yield strength and declined the elongation, but it did not have a considerable impact on the tensile strength. Furthermore, aging heat treatment caused the tensile properties to deteriorate and changed the fracture to a mixture of transgranular ductile and intergranular brittle mode.

Key words: nickel alloys; additive manufacturing; direct energy deposition; heat treatment; microstructure

1 Introduction

Nowadays, metal additive manufacturing (MAM) method has been introduced as a unique and interesting manufacturing technology to produce new materials and prototype parts. In this process, various intensive energy sources such as laser, electron beam and electric arc are employed to deposit several layers of molten metal [1−14]. In wire arc additive manufacturing (WAAM) process, electric arc and wire are used as the heat source and feedstock material, respectively. The electric arc is usually delivered by gas metal arc welding (GMAW), plasma arc welding (PAW) and gas tungsten arc welding (GTAW) processes [15−19]. The most important advantages of arc welding processes are the high deposition rate, the ability to produce large parts and the low capital investment [20,21]. Meanwhile, the production of parts with rough surfaces and poor dimensional accuracy are the main drawbacks of these processes. In addition, their high corresponding heat input can cause grain growth and the formation of detrimental phases in the microstructure of the final part which may deteriorate its mechanical properties [17,19]. Therefore, it is necessary to obtain the correlations between MAM process parameters and properties of the product. In this regard, many researchers have tried to find logical relationships between parameters of different MAM methods and microstructure/mechanical properties of various engineering alloys such as Ti−6Al−4V [16,22], stainless steels [15], Ni-based alloys [21], and Al alloys [23,24]. Among these materials, Ni-based Inconel 625 alloy has attracted much attention in MAM. It is a solid solution-strengthened high temperature alloy with special applications in

Corresponding author: Mahmood SHARIFITABAR; Tel: +98-5431132642; Fax: +98-5433447092; E-mail: msharifitabar@eng.usb.ac.ir
DOI: 10.1016/S1003-6326(20)65439-5

aerospace and marine industries [17,25−27]. It was previously shown that mechanical properties of Inconel 625 strongly depend on the type of MAM process. The optimum tensile strength of the as-prepared alloy fabricated by laser powder bed fusion (LPBF) varied between 900 and 1040 MPa [28], while it was lower than 800 MPa for the same alloy produced by arc welding processes such as GTAW and PAW [17,29]. In some cases, post-processing heat treatments were applied to improving the tensile strength of this alloy. MARCHESE et al [28] showed that direct aging of Inconel 625 alloy part produced by LPBF at 700 °C for 24 h increased the ultimate tensile strength (UTS) from 1041 to 1221 MPa. Also, solution heat treatment at 1150 °C for 2 h decreased UTS to 883 MPa and increased elongation from 33% to 55%, which confirmed the great influence of heat treatment on mechanical properties.

GMAW process is a promising candidate for MAM because of its very high deposition rate, the capability of automation and proper weld metal protection by inert gas [30,31]. Many studies have been concentrated so far on evaluating micro-structure and mechanical properties of various additively-manufactured alloys fabricated by GMAW process [15,16,27,30]. However, there is a lack of information on the properties of Inconel 625 alloy parts produced by this process. Recently, WANG et al [27] have investigated the effects of torch travel speed on microstructure and mechanical properties of Inconel 625 alloy fabricated by cold metal transfer wire arc additive manufacturing (CMT-WAAM) method. They showed that mechanical properties, except for UTS, were superior to those of the cast alloy. Nevertheless, it is worth noting that cold metal transfer gas metal arc welding (CMT-GMAW) process differs from the traditional GMAW process. In CMT-GMAW, the total heat generated by the arc is controlled via the pulsed feeding of the wire to the weld pool. This results in lower heat input to the manufactured part [32]. Consequently, it is expected that the properties of Inconel 625 alloy pieces manufactured by traditional GMAW differ from those produced by CMT-WAAM method. Furthermore, to the best knowledge of the authors, there is no report on the effects of post processing heat treatments on the microstructure and mechanical properties of Inconel 625 alloy parts manufactured by WAAM in the open literature. Thus, the aims of the present study were characterizing the microstructure and mechanical properties of Inconel 625 parts manufactured by GMA-WAAM method and investigating the effects of solution and aging heat treatments on the microstructure and mechanical properties of the manufactured parts.

2 Experimental

2.1 Materials

In order to prepare Inconel 625 walls by WAAM method, Ni−Cr−3Mo welding wire with 0.8 mm in diameter was purchased from ESAB Company. The substrate was surface-cleaned 304L stainless steel (SS) plate with the dimensions of 250 mm × 20 mm × 4 mm. The chemical compositions of the feeding wire (ESAB), the stainless steel substrate (measured by optical emission spectrometer, Oxford) and a common Inconel 625 alloy according to ASTM B443 standard are listed in Table 1. In addition, argon gas with the purity of 99.999% was used to inhibit weld metal oxidation during welding.

2.2 Fabrication conditions

Gas metal arc welding apparatus (JOUSHA S-MIG−303C) with direct current electrode positive (DCEP) polarity was used to deposit the weld metal, layer by layer. At first, some single-pass overlays were deposited with different welding parameters including welding current of 70−110 A, welding

Table 1 Chemical compositions of Inconel 625 welding wire, 304L stainless steel (SS) substrate and standard composition of Inconel 625 alloy

Material	Chemical composition/wt.%													Source
	C	Si	Mn	Cr	Ni	Mo	Cu	Al	Ti	Fe	V	S	P	
Inconel 625 wire	<0.1	<0.5	<0.5	21.5	Bal.	<0.5	0.5	0.4	0.4	0.2	−	−	−	ESAB
304L SS substrate	0.02	0.3	1.5	18.4	8.2	0.1	0.3	0.1	−	Bal.	0.1	0.01	0.03	Measured
Inconel 625 alloy	<0.1	<0.5	<0.5	20.0−23.0	>58	8.0−10.0	−	−	−	<5.0	−	−	−	ASTM B443

speed of 3.3−4.6 mm/s, and wire feeding rates of 9.5 and 11.5 m/min. The proper welding conditions were selected through the visual inspection of deposits to attain a uniform and defect-free weld track. Thereafter, 200 mm in length and 70 mm in height walls with 27 overlay welding passes were fabricated using the welding parameters listed in Table 2. The argon gas flow rate was adjusted to 15 L/min during welding. Each pass was deposited in opposite direction to the previous one with 3 min interval between subsequent passes to decrease the maximum inter-pass temperature to 150 °C. Macrograph of the wall is shown in Fig. 1(a). Three similar walls were fabricated. One of them was characterized in the as-prepared condition (AW), while the others were subjected to post-processing heat treatment and subsequent characterization. Moreover, a separate wall was fabricated with 6 overlay passes for microstructural characterization.

Table 2 WAAM process parameters

Welding parameter	value
Current/A	100
Voltage/V	18
Welding speed/(mm·s^{-1})	4.6
Argon gas flow rate/(L·min^{-1})	15
Wire feeding rate/(m·min^{-1})	9.5
Welding heat input/(J·mm^{-1})	386

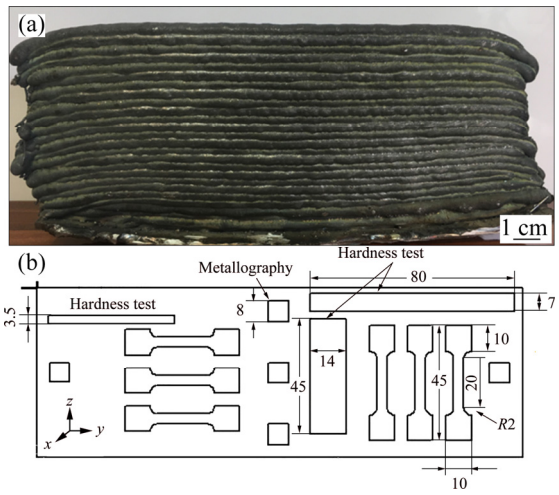

Fig. 1 Optical macrograph of Inconel 625 wall fabricated by WAAM (a) and schematic illustration of various specimens extracted from wall for characterization (b) (Unit: mm)

2.3 Heat treatment of walls

In order to obtain a uniform microstructure, two walls were solution heat treated (S) at (1100±5) °C for 6 h in an electric furnace and subsequently quenched in water. To prevent the alloy from oxidation, the walls were placed in a closed steel cup covered with a layer of charcoal. After that, one of them was aged (SA) at 700 °C for 24 h and then quenched in water. The heat treatment temperatures were almost similar to the optimum conditions reported by MARCHESE et al [28] during heat treatment of Inconel 625 walls fabricated by LPBF, while the solution heat treatment time increased up to 6 h.

2.4 Characterization

The structure of the walls was characterized by X-ray diffraction (Bruker advance D8) method with Cu K_α radiation. Microstructures of the walls at different locations were observed by optical (Olympus) and field emission scanning electron (FESEM MIRA3 TESCAN) microscopes equipped with energy dispersive spectroscopy (EDS SAMX) analyzer. Metallographic samples were polished with 1 μm diamond paste. To reveal microstructural features, as-prepared samples were electro-etched with chromium trioxide solution (90 mL H_2O and 10 g CrO_3) for 20 s. Also, electro-etching in 20% oxalic acid solution for 45 s was used for heat treated samples. Mechanical properties were evaluated by room temperature tensile test in both welding (x-axis) and building (z-axis) directions. Location and dimensions of tensile specimens are shown in Fig. 1(b). Six sub-size tensile test specimens were extracted from each wall due to the small size of the walls; three of them are along the welding direction and the others are along the building direction. Then, the average value of the three samples was reported. The dimensions of the specimens were similar to those reported by WANG et al [29]. The test was performed by universal tensile testing machine (GOTECH, Taiwan, China) with a cross head speed of 5 mm/min. In addition, Vickers microhardness test (INNOVA TEST) with 500 g load for 10 s was used to assess the hardness variation along both x and z axes. For each condition, the mean value of 20 measuring points was reported.

3 Results and discussion

3.1 Chemical composition and phase constitution

The high heat input of the GMA welding process may evaporate some alloying elements and change the chemical composition of the weld metal. Therefore, the composition of the as-prepared wall was measured by optical emission spectrometer. Accordingly, it contains 22.2% Cr, 9.3% Mo, 3.7% Nb, 0.17% Ti, 0.18% Fe, 0.05% Si, 0.06% Co, 0.05% Al, 0.02% C, 0.02% V, and balance Ni (all in wt.%) which is completely consistent with the composition of Inconel 625 alloy reported by the ASTM B443 standard in Table 1.

X-ray diffraction (XRD) patterns of the as-prepared (AW), solution heat treated (S), and solution and aged (SA) samples are shown in Fig. 2(a). Nickel-based solid solution (00-003-1016) with FCC crystal structure was only detected in all the samples. As shown in Fig. 2(b), the peak corresponding to the (111) plane in the as-prepared wall (AW) at 2θ=43.73° shifted to the lower diffraction angle of 2θ=43.31° after solution heat treatment (S), while it shifted to the higher angle of 43.55° after aging heat treatment. This change in the XRD peak position may be due to the variation of the lattice parameter of the Ni-FCC structure. The calculation of the lattice parameter by the Bragg's equation showed that it increased from 0.3586 nm in the as-prepared sample to 0.3614 nm after homogenization heat treatment. This can be due to the dissolution of segregated alloying elements in the Ni-based matrix. However, the lattice parameter of the aged sample slightly decreased to 0.3604 nm, most probably as a result of γ'' (Ni_3Nb) precipitation which takes out the atoms, especially Nb, from the solid−solution structure. More details on the microstructural changes are represented in the following section. It is worth noting that the XRD peak shift may also occur as a result of residual stresses. However, in the present study, small XRD samples with the dimensions of 10 mm × 10 mm × 3 mm were extracted from the walls which can lead to the relaxation of stresses.

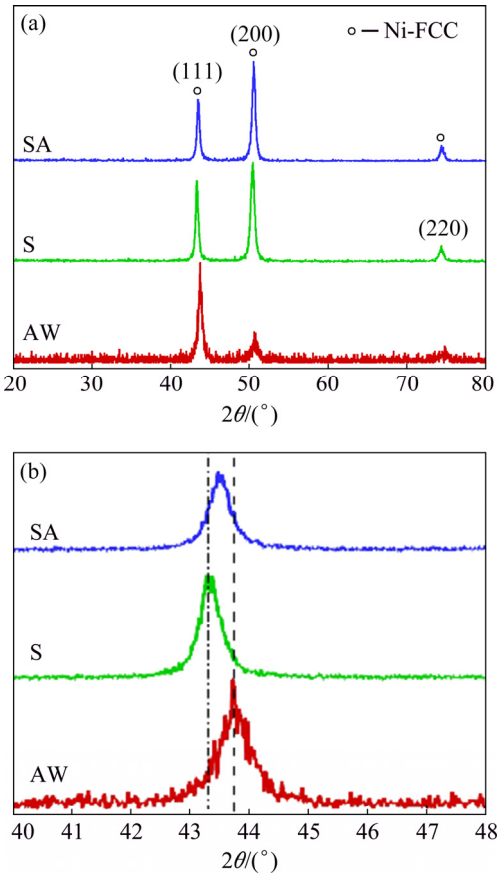

Fig. 2 X-ray diffraction patterns of as-prepared (AW), solution heat-treated (S), and solution and aged (SA) samples (a) and changes of (111) peak position after heat treatment (b)

3.2 Microstructure

3.2.1 As-prepared sample

In metal additive manufacturing methods like WAAM, a desired part is made by overlapping the weld metal layer by layer, in which the solidification microstructure, the grain size and the orientation depend strongly on the location of the deposited layer relative to the substrate and the scanning strategy of the layers [29,33]. According to the solidification theory of weld metal, most grains grow perpendicularly to the weld pool interface because they chase the heat flux direction with the maximum temperature gradient [34,35]. This leads to a preferred grain orientation in the manufactured parts, resulting in anisotropy in the mechanical properties. Figure 3(a) shows optical macrograph of wall with 1.6 cm in height fabricated with 6 overlay passes. The layers are well-defined and can easily be distinguished in this figure. The deposited wall is completely sound and free from any welding defect like crack and porosity in each layer and between two subsequent layers. Optical micrographs of the weld metal at different locations of the wall are shown in Figs. 3(b−g). There is an intimate and good metallurgical bond between the

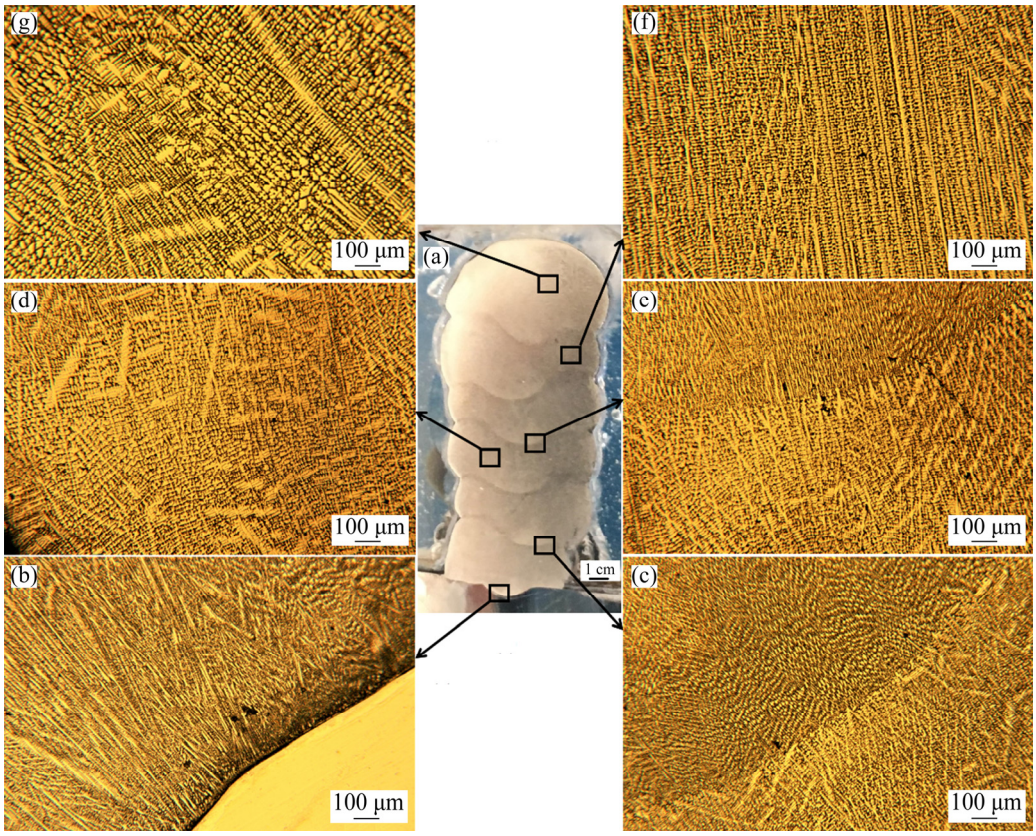

Fig. 3 Optical macrograph of 6-layer wall manufactured by WAAM (a) and optical micrographs of wall at different locations (b−g)

weld metal and 304L stainless steel substrate, as shown in Fig. 3(b). The microstructure of the weld metal near the interface contains a mixture of cellular and dendritic grains with very fine secondary arms. Most dendrites have grown toward the preferential *z*-axis which is almost perpendicular to the substrate interface. Despite the epitaxial growth of some grains between the layers in Figs. 3(c) and (e), there is a sharp change in the grain structure at the layers interface, most probably due to the melting of previous grains in the deposited layer by the next pass and their resolidification. The secondary dendrite arm spacing (SDAS) increases with increasing the wall height from (6±2) μm near the interface to (15±3) μm at the top. The solidification microstructure depends on the solidification rate (R), temperature gradient (G), and melt composition. It is well understood that the type of grain structure is determined by G/R ratio, while the size of the solidification structure is governed by GR product [35]. The morphology of the solidification structure varies from cellular to dendritic by decreasing the G/R ratio. Moreover, the higher cooling rate (i.e. high G and R) results in finer microstructure [35]. Upon depositing the first layer, the substrate acts as a heat sink which increases the temperature gradient and cooling rate. Therefore, fine cellular grains formed near the substrate. However, heat accumulation in the top layers decreased the temperature gradient and solidification rate, altered the grain structure from cellular to dendritic, and considerably increased the SDAS.

To manufacture a desired part by WAAM, the weld metal was deposited on the previous solidified layer. Therefore, the heat released by the next pass might change the microstructure of the previous one. Figures 4(a) and (b) show FESEM images of the reheated region and the last deposited layer of wall, respectively. In both regions, some secondary phases with bright color contrast were formed in the inter-dendritic region. The mean size and volume fraction of the secondary particles measured by Image J software were 6.7 μm and 3.0%, respectively, in the top layer. However, they increased to 8.4 μm and 3.7% in the reheated region. The calculated volume fraction of the secondary

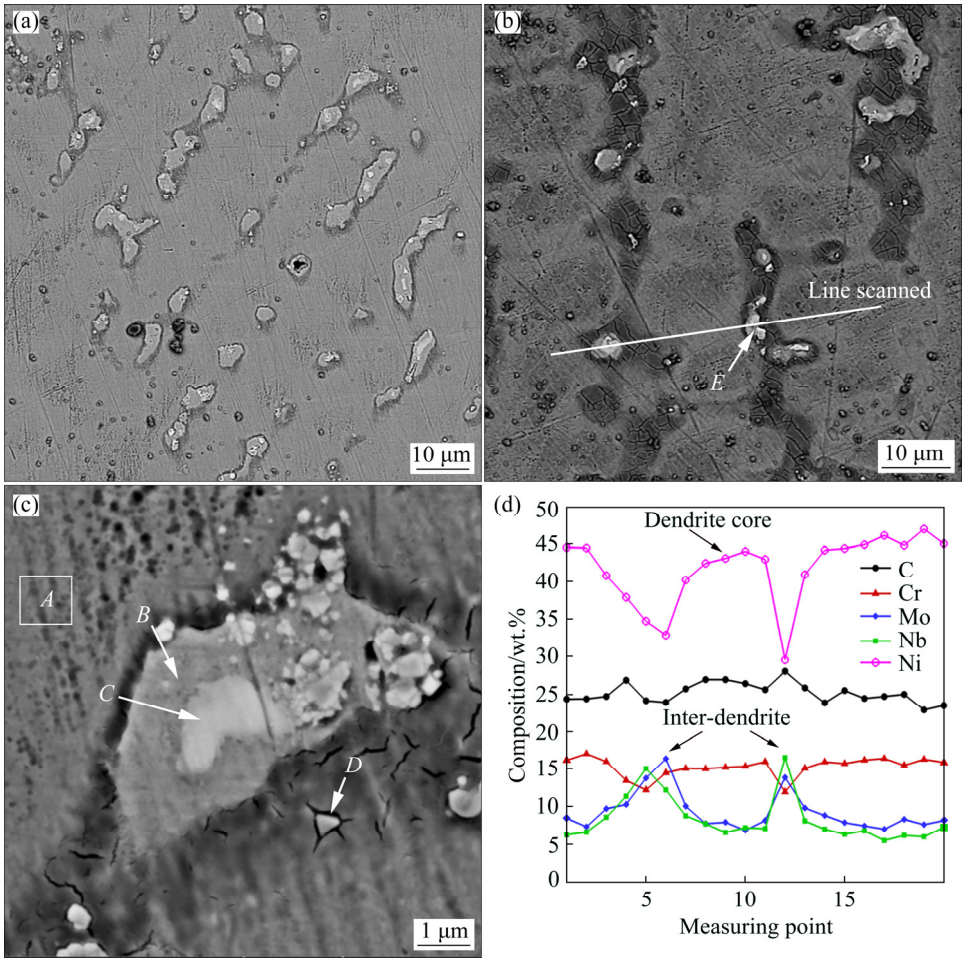

Fig. 4 FESEM images of Inconel 625 alloy produced by WAAM in reheated region (a) and last overlay pass (b) and micrograph with higher magnification of secondary phases formed in interdendritic region (c) and EDS line scan (d) along line shown in (b)

particles was lower than the detection threshold of the XRD instrument, i.e. about 5%. Meanwhile, it seems that the slight increase in the size and volume fraction of particles occurred by subsequent heating in the reheating region. Change in the morphology and volume fraction of secondary phases with wall height during gas tungsten arc additive manufacturing of Inconel 625 alloy was reported by WANG et al [29].

To investigate the distribution of the alloying elements in the microstructure, the EDS line scan along the line shown in Fig. 4(b) is illustrated in Fig. 4(d). It can be seen that most of the alloying elements were distributed non-uniformly with severe segregation. The dendrite core was enriched in Ni and Cr, while the interdendritic regions had high contents of Mo, Nb and C. Therefore, it seems that the segregation of the latter elements in the interdendritic region led to the formation of some secondary phases.

The micrograph of the secondary phases at higher magnification is shown in Fig. 4(c). Moreover, semi-quantitative chemical composition of these phases and the matrix measured by the EDS analysis are listed in Table 3. The content of C was not reported because of the EDS instrumental limitation for semi-quantitative measurement of light elements. The matrix (Point *A*) is a Ni-based solid solution containing Cr, Nb, Fe and Mo. The formation of Ni-based solid solution was confirmed by XRD analysis. Secondary phases appeared with different morphologies and color contrast in the FESEM image shown in Fig. 4(c). There were some fine white particles (marked as *D*) with regular shape. Moreover, in some areas, a bright irregular phase (Point *C*) was surrounded by a light gray phase (Point *B*). The white particles (marked as *D*) enriched in Nb, Mo and Ti were (Nb,Mo,Ti)C carbide. The contents of Nb and Mo were higher at Points *B* and *C* than those of the matrix at Point *A*.

Table 3 EDS semi-quantitative chemical compositions of various phases shown in Fig. 4

Analyzed point	Chemical composition/at.%					
	Cr	Fe	Ni	Nb	Mo	Ti
A	25.1	2.6	60.4	4.6	7.3	−
B	23.0	0.5	58.3	8.6	9.6	−
C	19.0	1.5	43.8	20.4	15.3	−
D	12.3	0.9	26.1	48.4	9.2	3.1
E	21.7	0.3	47.6	16.8	13.6	−

XU et al [17] extensively investigated the type of secondary phases formed during plasma arc additive manufacturing of Inconel 625 alloy by transmission electron microscopy (TEM) and the EDS analyses. They showed that intermetallic phases such as Laves phase, δ-Ni_3Nb, and MC carbides formed in the deposited structure. The Laves phase had an A_2B structure (A: Ni, Cr, Fe; B: Nb, Mo, Ti). According to these researchers, solidification of the alloy started with $L\rightarrow\gamma$ transformation. Then, MC carbide was formed by subsequent $L\rightarrow\gamma$ + MC eutectic reaction. Finally, the rest of the liquid was solidified by $L\rightarrow\gamma$ + Laves + δ ternary eutectic reaction. In addition, they showed that more δ-phase was formed in the top region of the wall and reheated zone than near the substrate interface. Therefore, they concluded that as the heat input of the manufacturing process increased, the accumulation of alloying elements in the interdendritic region promoted the formation of δ-Ni_3Nb phase. Moreover, reheating led to the dissolution of Laves phase and the precipitation of δ-Ni_3Nb phase during subsequent cooling [17]. The formation of Laves phase was similarly reported by WANG et al [29] during gas tungsten arc additive manufacturing of Inconel 625 alloy. As listed in Table 3, the bright phase marked as Point *C* had Ni+Cr+Fe of 64.3 at.% and Nb+Mo+Ti of 35.7 at.% which accords with the A_2B structure of Laves phase. Point *E* in Fig. 4(b) had a similar composition as listed in Table 3. On the other hand, the light gray phase around the Laves phase contains Ni+Cr+Fe of 81.8 at.% and Nb+Mo+Ti of 18.2 at.% that is similar to the composition of δ-$(Ni,Cr,Fe)_3(Nb,Mo)$ phase. So, it can be concluded that besides Ni-based solid solution, MC carbide, Laves phase and δ-phase were formed in the structure of the as-prepared wall.

3.2.2 Heat-treated samples

Mechanical properties of Inconel 625 alloy are improved by solid solution strengthening mechanism [36]. However, the severe segregation occurring during solidification led to the formation of carbide, Laves phase and δ phase in the interdendritic region of the as-prepared samples. Moreover, the directional solidification in the weld pool may result in anisotropy in the mechanical properties. To obtain a more uniform microstructure, solution heat treatment was performed at 1100 °C for 6 h. Thereafter, one sample was aged at 700 °C for 24 h to explore the effect of aging heat treatment on microstructure and mechanical properties of the alloy. Figures 5(a) and (b) show FESEM images of the solution heat-treated sample taken from *xy* and *xz* planes, respectively. The solidification microstructure completely disappeared and most of the secondary phases were dissolved in the matrix. The new grains in the *xy* plane were almost equiaxed (Fig. 5(a)), while they were elongated along the dendrite growth direction in the *xz* plane (Fig. 5(b)). This seems that the solution heat treatment could not completely remove the microstructural anisotropy. The magnified micrograph of this sample in Fig. 5(c) indicated that there exist some secondary bright particles in the grains in addition to at the grain boundaries. EDS spectra of these particles are shown in Figs. 6(a) and (b). High contents of Nb, Ti and C confirm that they are MC carbide particles remained after solution heat treatment. Aging heat treatment did not have considerable effect on the grain size, but it led to the formation of a discontinuous phase at grain boundaries, as shown in Figs. 5(d) and (e). Moreover, nanometric γ'' particles precipitated in the microstructure.

The FESEM image with very high magnification taken from the nanoprecipitates with the sizes of 10−30 nm is shown in Fig. 5(f). As illustrated, the non-uniform distribution of nanoprecipitates led to the formation of some precipitation-free zones (PFZs), especially close to the grain boundaries, as shown in Fig. 5(e). The EDS spectrum of the grain boundary phase in Fig. 6(c) confirmed that it is enriched in Cr and C elements and therefore, it is $M_{23}C_6$ carbide phase [28]. Figure 6(d) also shows the EDS spectrum of the matrix having high content of Ni

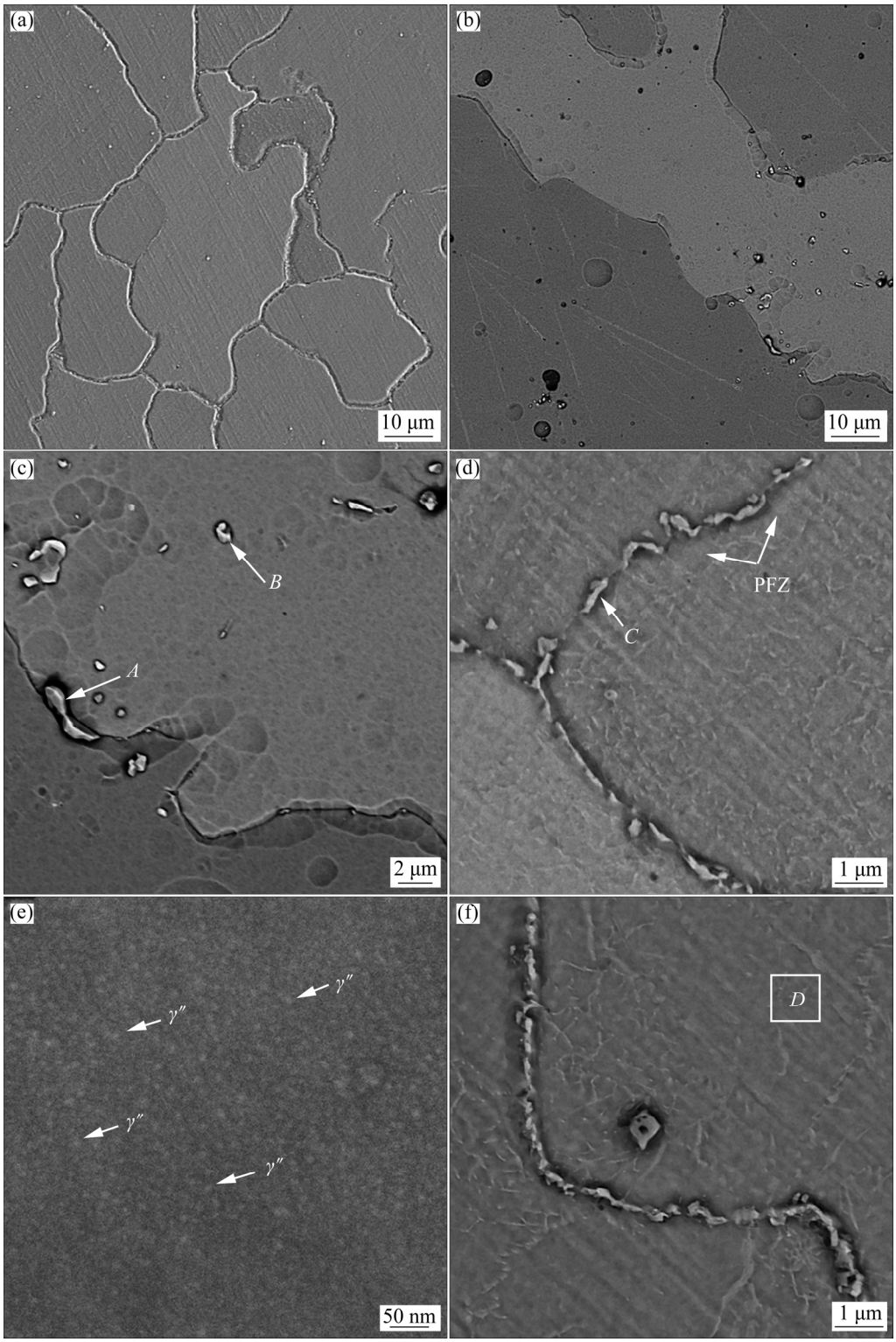

Fig. 5 FESEM images of different samples: (a, b) Solution heat-treated sample taken from *xy* and *xz* planes, respectively; (c) Higher magnification of solution heat-treated sample; (d, e) Aged sample; (f) High magnification of aged sample containing nanometric precipitates

originated from the γ solid solution phase. According to the isothermal transformation diagram of Inconel 625 alloy [37], solution heat treatment above 1000 °C dissolves most of the compounds like δ and Laves phases, γ'' precipitates, and $M_{23}C_6$ carbide [38]. However, MC and M_6C carbides are stable up to 1100 °C. During aging at 700 °C, $Cr_{23}C_6$ and γ'' phases can form at short time less

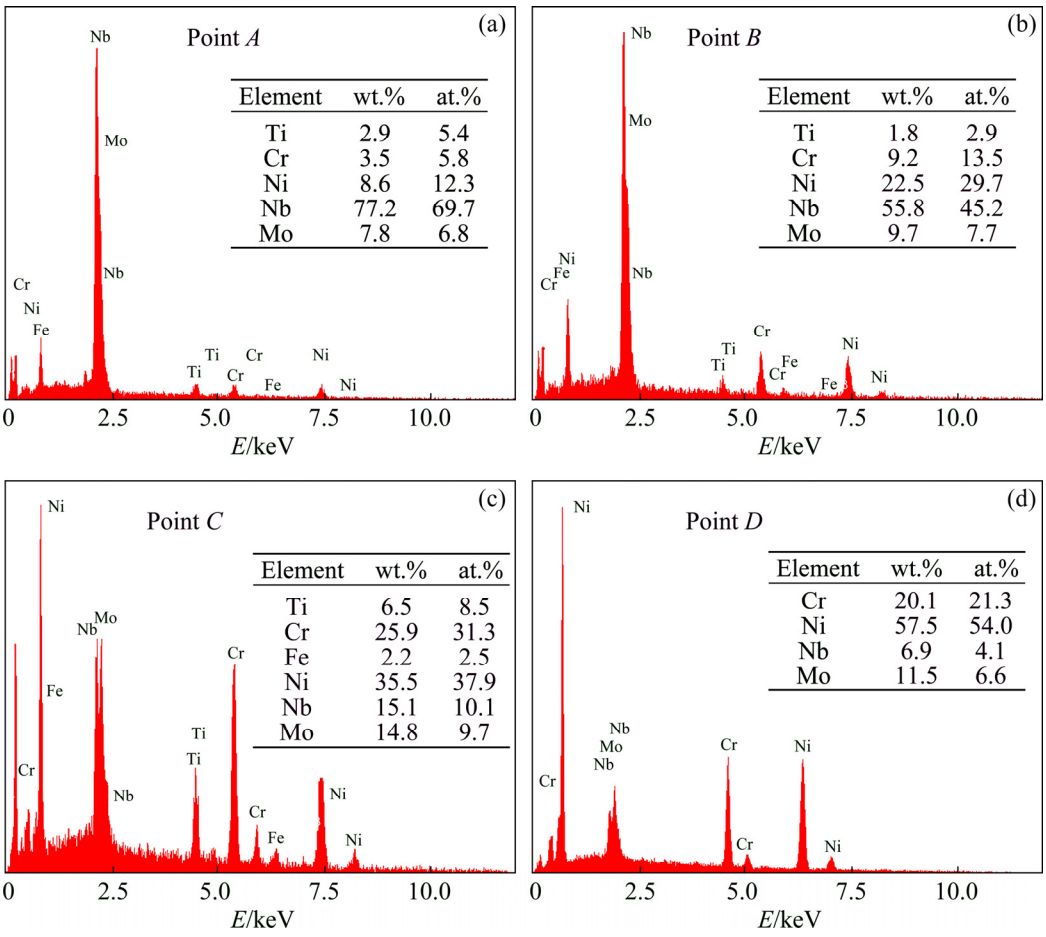

Fig. 6 EDS spectra of various phases marked in Fig. 5

than 10 h, while the formation of Laves and δ phases needs prolonged time higher than 20 h. Therefore, as shown in Figs. 5(a−c), Laves and δ phases were dissolved after solution heat treatment and only MC and M_6C carbides remained in the microstructure. On the other hand, aging heat treatment led to the formation of $M_{23}C_6$ carbide along the grain boundaries and γ'' precipitates within the grains. These results were completely consistent with the isothermal transformation diagram of the alloy [37]. Nevertheless, it seems that the solution heat treatment time and/or temperature was not high enough to obtain a uniform distribution of alloying elements in the microstructure. Moreover, the formation of carbides resulted in lower contents of some alloying elements, especially Nb, in some parts of the matrix. Accordingly, γ''-Ni_3Nb nanometric precipitates were developed only in those regions with high alloying element contents, where most were probably the dissolution areas of Laves and δ phases. Conversely, the PFZs were formed in those regions with low alloying element contents. In other words, the formation of MC carbide at the grain boundaries resulted in the formation of PFZs at their vicinity. In a similar study, XU et al [17,33] reported the formation of PFZ near the grain boundary carbides for Inconel 625 alloy manufactured by pulsed plasma arc additive manufacturing method. MARCHESE et al [28] investigated the effect of solution and aging heat treatments on microstructure and mechanical properties of Inconel 625 walls produced by laser powder bed fusion (LBF). They showed that fine dendritic grains with intergranular Laves phase were formed in the microstructure of as-prepared alloy. Solution heat treatment at 1150 °C for 1 h resulted in the dissolution of Laves and δ phases. As a result, a uniform distribution of γ'' precipitates was obtained after aging of this sample at 700 °C for 24 h. Moreover, $M_{23}C_6$ carbide particles were developed at the grain boundaries. However, the high cooling

rates of the LBF process hindered severe alloying element segregation during solidification. In addition, fine dendritic microstructure with primary dendrite arm spacing (PDAS) of 1 μm decreased the diffusion distance and accelerated the homogenization process. In comparison to LBF, the high heat input of the GMA welding process and its lower cooling rate led to the formation of coarse dendritic microstructure with the mean PDAS of 40 μm, secondary dendrite arm spacing (SDAS) of (15±3) μm and high segregation level of Nb and Mo elements to the interdendritic region. As a result, intermediate Laves and δ phases with large particle size were formed in the microstructure of the as-prepared sample. Complete homogenization during solution heat treatment did not occur due to the large diffusion distance of atoms which resulted in the non-uniform distribution of γ'' nanoprecipitates (Ni_3Nb) after aging heat treatment.

3.3 Mechanical properties

Table 4 lists some mechanical properties of the as-prepared and heat-treated Inconel 625 walls fabricated by WAA method. Moreover, the obtained results were compared with the properties of Inconel 625 alloy processed by other metal additive manufacturing methods, as well as the as-cast alloy. Both yield and tensile strengths of as-prepared samples were slightly higher in the travel direction (TD) along the *x*-axis than those in the building direction (BD) along the *z*-axis, while their elongation was similar. Moreover, the tensile strength and elongation of the alloy in the building direction were close to those of the as-cast alloy. However, the yield strength was considerably higher in the case of WAA manufactured alloy, most probably due to the finer grain structure obtained by higher cooling rate of this method compared to the casting process. Yield strength and hardness increased after solution heat treatment, while tensile strength remained almost constant and elongation decreased. The increase in the yield strength and hardness may be attributed to the dissolution of unwanted Laves and δ phases in the matrix and subsequent solid solution strengthening mechanism of the dissolved elements. Aging of the solution heat-treated sample not only declined tensile and yield strengths, but also dramatically decreased the elongation. However, it didn't have any influence on hardness. As mentioned previously, γ'' precipitates were formed after aging. Thus, solid solution strengthening mechanism was replaced by precipitation hardening mechanism and hardness remained almost constant. Meanwhile, the non-uniform distribution of precipitates, as well as the establishment of grain boundary carbide led to the development of PFZs with low contents of alloying elements, especially near the grain boundaries. Moreover, previous studies confirmed that the formation of $Cr_{23}C_6$ carbide at the grain boundaries had detrimental influence on the mechanical properties and especially elongation of

Table 4 Comparison of mechanical properties of WA additively manufactured Inconel 625 alloy in present study with those of alloys prepared by other additive manufacturing processes

Fabrication technique	Test direction	Yield strength/MPa	Tensile strength/MPa	Elongation/%	Hardness (HV)
GMAW-AW	TD	444±13	704±10	47±2	244±21
	BD	433±8	673±13	47±1	249±27
GMAW-S	TD	466±18	705±12	38±6	302±22
	BD	468±7	667±13	41±3	306±10
GMAW-SA	TD	438±15	640±24	32±4	297±10
	BD	458±5	648±18	37±5	307±16
GTAW [29]	TD	−	722±17	42±2	−
	BD	−	684±23	40±4	−
CMT-GMAW [27]	BD	389±12	670±20	44±2	−
	TD	375±9	628±12	−	−
PAW [17,33]	−	390−500	690−754	45−49	−
Casting	−	350	710	48	−

the alloy [28,37]. Therefore, yield strength, tensile strength, and the elongation of the alloy declined after aging heat treatment.

Tensile properties of the Inconel 625 alloy part fabricated in the present work were comparable with those of the same alloy parts produced by other WAAM methods like GTAW, CMT-GMAW and PAW [17,27,29,33]. However, in the case of LPBF process, the strength was considerably higher at the expense of elongation. Mechanical properties are mainly affected by microstructural features. In the case of arc welding processes, similar cooling rate of the manufactured part led to the analogous microstructures and mechanical properties. However, very fast cooling rate of the LPBF process not only reduced the extent of the segregation during solidification, but also led to the formation of very fine dendrites [5,25]. As a result, tensile strength of the alloy fabricated by LPBF process was considerably higher than that of the alloy fabricated by arc welding processes. Nevertheless, the formation of pores declined formability of the alloy produced by LPBF technique.

3.4 Fracture surface characterization

Fracture surfaces of tensile test specimens were characterized by FESEM to explore the fracture mechanism. FESEM images with different magnifications showing the fracture surface of various specimens tested on both welding (*x*-axis) and building (*z*-axis) directions are illustrated in Fig. 7. Despite some large dimples, the almost uniform distribution of fine dimples confirms the transgranular ductile fracture mode of the as-prepared sample in both building and welding directions, as shown in Figs. 7(a) and (b), respectively. For the sample tested along the building direction (*z*-axis), dimples were formed in parallel bands. The higher magnification micrograph taken by backscattered electron (BSE) imaging mode is inserted in Fig. 7(a). It shows that the dimples were originated from some secondary particles (Point *A*) having brighter color contrast than the matrix (Point *B*). The EDS semi-quantitative chemical compositions of a particle and the matrix are listed in Table 5.

Particles with high contents of both C and carbide forming elements like Nb and Ti can be estimated as MC carbide phase, while the matrix is a Ni-based solid solution having high content of Cr. It was previously shown that dendrites grew mainly along the *z*-axis. For the specimen loaded on the *x*-axis, tensile stress was exerted normal to the dendrite growing direction. As a result, dimples originated from the secondary particles were formed sequentially along the dendrite axes. Fracture surfaces of the specimens tested on both building (*z*-axis) and welding (*x*-axis) directions after solution heat treatment are shown in Figs. 7(c) and (d), respectively. The fracture mode is completely ductile with fine dimples.

Solution heat treatment led to the dissolution of secondary phases and resulted in appropriate distribution of alloying elements in the matrix. It was previously confirmed that the size of dimples in ductile fracture mode depends on tensile strain rate, temperature, properties of the materials, and the size and distribution of secondary particles [39]. Both the as-prepared and solution heat-treated samples had similar strength. However, the size of dimples in solution heat-treated specimen ((2.7±0.4) μm) was lower than that in as-prepared one ((3.6±0.5) μm). By considering the same testing conditions for both mentioned samples, this difference could be related to the large size and non-uniform distribution of secondary phases like carbides, Laves and δ phases in the microstructure of the as-prepared alloy. The fracture surfaces of the solution heat-treated and subsequently aged samples are shown in Figs. 7(e) and (f). In addition to transgranular dimples, there are signs of brittle fracture mode as shown by white arrows in Fig. 7. The brittle fracture may originate from the grain boundary carbide formed after aging heat treatment. It was previously shown that the formation of grain boundary carbide considerably decreased the elongation of the alloy. In a similar study, MARCHESE et al [28] showed that the formation of $Cr_{23}C_6$ carbide after aging heat treatment led to a mixture of ductile and brittle fracture modes in the Inconel 625 alloy manufactured by LPBF. Finally, it can be concluded that the fracture in the as-prepared and solution heat-treated conditions occurred mainly in a transgranular ductile mode. However, the formation of $Cr_{23}C_6$ carbide at grain boundary after aging heat treatment led to lower elongation because it facilitated the growth of the cracks along the grain boundaries.

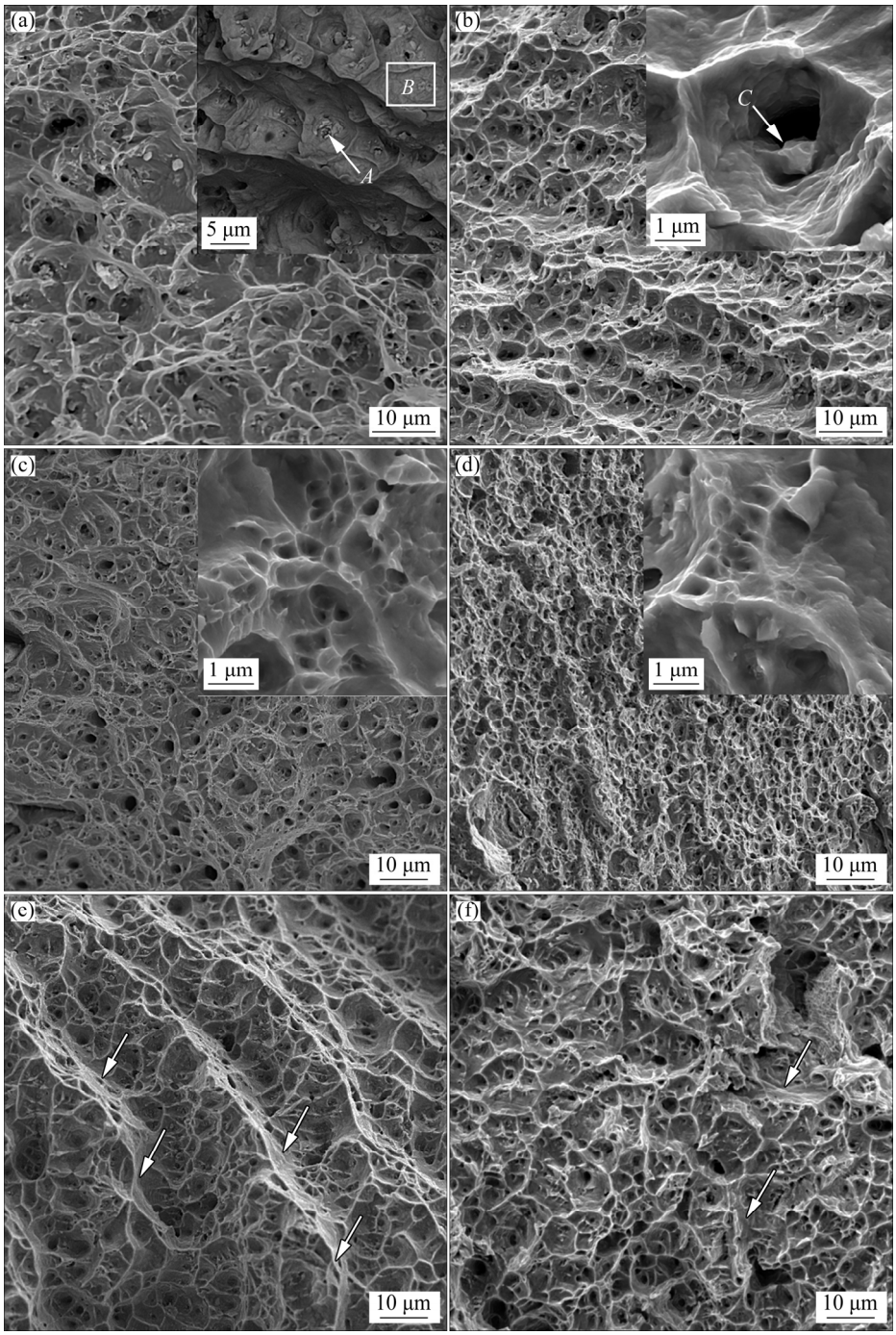

Fig. 7 FESEM images of fracture surfaces at different magnifications in as-prepared samples tested along *z*-axis (a) and *x*-axis (b), solution heat-treated samples tested along *z*-axis (c) and *x*-axis (d), and solution heat-treated and aged samples tested along *x*-axis (e) and *z*-axis (f)

Table 5 EDS semi-quantitative chemical compositions of different phases marked in Fig. 7

Analyzed point	Chemical composition/wt.%						
	C	Cr	Fe	Ni	Nb	Mo	Ti
A	21.0	4.0	−	11.8	62.7	−	0.5
B	−	22.5	−	64.5	4.2	8.6	0.2
C	30.5	10.3	0.3	25.9	31.6	16.1	1.4

4 Conclusions

(1) For Inconel 625 alloy walls, the formation of dendritic microstructure with considerable segregation of Nb and Mo alloying elements in the interdendritic region resulted in the formation of

NbC, Laves and δ-Ni_3Nb phases. Solution heat treatment at 1100 °C led to the dissolution of Laves and δ phases and removal of dendritic microstructure. Aging heat treatment at 700 °C for 24 h resulted in the formation of $M_{23}C_6$ carbide at the grain boundaries and uneven distribution of nanometric γ'' precipitates in the microstructure.

(2) Mechanical properties of the as-prepared alloy were comparable to those of the as-cast alloy and the same alloy fabricated by other WAAM methods like CMT-GMAW and GTAW. Solution heat treatment improved hardness and yield strength and decreased elongation while it did not have any considerable influence on tensile strength. On the contrary, aging heat treatment declined all the mechanical properties.

(3) Fracture in the as-prepared and solution heat-treated samples occurred in a transgranular ductile mode. However, the size of dimples decreased considerably after solution heat treatment. On the other hand, a mixture of transgranular ductile and intergranular brittle fracture mode was observed in the aged sample due to the formation of $Cr_{23}C_6$ carbide at grain boundary.

Data availability statement

The raw/processed data required to reproduce these findings cannot be shared at this time as the data also forms part of an ongoing study.

Acknowledgments

The authors acknowledge Mr. A. R. Gardeshzadeh for proofreading of the manuscript.

References

[1] MURR L E. Metallurgy of additive manufacturing: Examples from electron beam melting [J]. Additive Manufacturing, 2015, 5: 40−53.

[2] LOH G H, PEI E, HARRISON D, MONZON M D. An overview of functionally graded additive manufacturing [J]. Additive Manufacturing, 2018, 23: 34−44.

[3] CUNNINGHAM C, FLYNN J, SHOKRANI A, DHOKIA V G, NEWMAN S T. Invited review article: Strategies and processes for high quality wire arc additive manufacturing [J]. Additive Manufacturing, 2018, 22: 672−686.

[4] ZHAI Y W, LADOS D A, BROWN E J, VIGILANTE G N. Understanding the microstructure and mechanical properties of Ti−6Al−4V and Inconel 718 alloys manufactured by laser engineered net shaping [J]. Additive Manufacturing, 2019, 27: 334−344.

[5] PLEASS C, JOTHI S. Influence of powder characteristics and additive manufacturing process parameters on the microstructure and mechanical behaviour of Inconel 625 fabricated by selective laser melting [J]. Additive Manufacturing, 2018, 24: 419−431.

[6] KNAPP G L, RAGHAVAN N, PLOTKOWSKI A, DEBROY A T. Experiments and simulations on solidification microstructure for Inconel 718 in powder bed fusion electron beam additive manufacturing [J]. Additive Manufacturing, 2019, 25: 511−521.

[7] MURR L E, GAYTAN S M, RAMIREZ D A, MARTINEZ E, HERNANDEZ J, AMATO K N, SHINDO P W, MEDINA F R, WICKER R B. Metal fabrication by additive manufacturing using laser and electron beam melting technologies [J]. Journal of Materials Science & Technology, 2012, 28: 1−14.

[8] LONG Yi-tong, NIE Pu-lin, LI Zhu-guo, HUANG Jian, LI Xiang, XU Xin-mei. Segregation of niobium in laser cladding Inconel 718 superalloy [J]. Transactions of Nonferrous Metals Society of China, 2016, 26: 431−436.

[9] ZHAO Zhuang, CHEN Jing, ZHANG Qiang, TAN Hua, LIN Xin, HUANG Wei-dong. Microstructure and mechanical properties of laser additive repaired Ti17 titanium alloy [J]. Transactions of Nonferrous Metals Society of China, 2017, 27: 2613−2623.

[10] CHEN Gang, ZHAO Shao-yang, TAN Ping, YIN Jing-ou, ZHOU Quan, GE Yuan, LI Zeng-feng, WANG Jian, TANG Hui-ping, CAO Ping. Shape memory TiNi powders produced by plasma rotating electrode process for additive manufacturing [J]. Transactions of Nonferrous Metals Society of China, 2017, 27: 2647−2655.

[11] ZHU Yan-yan, CHEN Bo, TANG Hai-bo, CHENG Xu, WANG Hua-ming, LI Jia. Influence of heat treatments on microstructure and mechanical properties of laser additive manufacturing Ti−5Al−2Sn−2Zr−4Mo−4Cr titanium alloy [J]. Transactions of Nonferrous Metals Society of China, 2018, 28: 36−46.

[12] ISMAEEL A, WANG C. Effect of Nb additions on microstructure and properties of γ-TiAl based alloys fabricated by selective laser melting [J]. Transactions of Nonferrous Metals Society of China, 2019, 29: 1007−1016.

[13] GUO Kuai-kuai, LIU Chang-sheng, CHEN Sui-yuan, DONG Huan-huan, WANG Si-yu. High pressure EIGA preparation and 3D printing capability of Ti−6Al−4V powder [J]. Transactions of Nonferrous Metals Society of China, 2020, 30: 147−159.

[14] LIU Zhan-qi, MA Rui-xin, XU Guo-jian, WANG Wen-bo, SU Yun-hai. Effects of annealing on microstructure and mechanical properties of γ-TiAl alloy fabricated via laser melting deposition [J]. Transactions of Nonferrous Metals Society of China, 2020, 30: 917−927.

[15] MARTINA F, DING J L, WILLIAMS S, CABALLERO A, PARADAL G, QUINTINO L. Tandem metal inert gas process for high productivity wire arc additive manufacturing in stainless steel [J]. Additive Manufacturing, 2019, 25: 545−550.

[16] WU B T, PAN Z X, DING D H, CUIUIR D, LI H. Effects of heat accumulation on microstructure and mechanical properties of Ti6Al4V alloy deposited by wire arc additive

manufacturing [J]. Additive Manufacturing, 2018, 23: 151−160.

[17] XU F J, LV Y H, LIU Y X, SHU F Y, HE P, XU B. Microstructural evolution and mechanical properties of Inconel 625 alloy during pulsed plasma arc deposition process [J]. Journal of Materials Science & Technology, 2013, 29: 480−488.

[18] LIN J J, LV Y H, GUO D J, WU X Y, LI Z, LIU C, GUO B G, XU G, XU B. Enhanced strength and ductility in thin Ti−6Al−4V alloy components by alternating the thermal cycle strategy during plasma arc additive manufacturing [J]. Materials Science and Engineering A, 2019, 759: 288−297.

[19] WU B T, PAN Z X, DING D H, CUIURI D, LI H J, XU J, NORRISH J. A review of the wire arc additive manufacturing of metals: Properties, defects and quality improvement [J]. Journal of Manufacturing Processes, 2018, 35: 127−139.

[20] WILLIAMS S W, MARTINA F, ADDISON A C, DING J L, PARDAL G, COLEGROV P. Wire + arc additive manufacturing [J]. Materials Science and Technology, 2016, 32: 641−647.

[21] DHINAKARAN V, AJITH J, FATHIMA YASIN FAHMIDHA A, JAGADEESHA T, SATHISH T, STALIN B. Wire arc additive manufacturing (WAAM) process of nickel based superalloys: A review [J]. Materials Today: Proceedings, 2020, 21: 920−925.

[22] SINGH S, RAMAKRISHNA S, SINGH R. Material issues in additive manufacturing: A review [J]. Journal of Manufacturing Processes, 2017, 25: 185−200.

[23] AYARKWA K, WILLIAMS S W, DING J. Assessing the effect of TIG alternating current time cycle on aluminium wire + arc additive manufacture [J]. Additive Manufacturing, 2017, 18: 186−193.

[24] LI Neng, HUANG Shuai, ZHANG Guo-dong, QIN Ren-yao, LIU Wei, XIONG Hua-ping, SHI Gong-qi, BLACKBURN J. Progress in additive manufacturing on new materials: A review [J]. Journal of Materials Science & Technology, 2019, 35: 242−269.

[25] GONZALEZ J A, MIRELES J, STAFFORD S W, PEREZ M A, TERRAZAS C A, WICKER R B. Characterization of Inconel 625 fabricated using powder-bed-based additive manufacturing technologies [J]. Journal of Materials Processing Technology, 2019, 264: 200−210.

[26] SHEN M Y, TIAN X J, LIU D, TANG H B, CHENG X. Microstructure and fracture behavior of TiC particles reinforced Inconel 625 composites prepared by laser additive manufacturing [J]. Journal of Alloys and Compounds, 2018, 734: 188−195.

[27] WANG Y F, CHEN X Z, SU C. Microstructure and mechanical properties of Inconel 625 fabricated by wire-arc additive manufacturing [J]. Surface and Coatings Technology, 2019, 374: 116−123.

[28] MARCHESE G, LORUSSO M, PARIZIA S, BASSINI E, LEE J W, CALIGNANO F. Influence of heat treatments on microstructure evolution and mechanical properties of Inconel 625 processed by laser powder bed fusion[J]. Materials Science and Engineering A, 2018, 729: 64−75.

[29] WANG J F, SUN Q J, WANG H Q, LIU J P, FENG J C. Effect of location on microstructure and mechanical properties of additive layer manufactured Inconel 625 using gas tungsten arc welding [J]. Materials Science and Engineering A, 2016, 676: 395−405.

[30] ZHOU Y H, LIN X, KANG N, HUANG W D, WANG J, WANG Z. Influence of travel speed on microstructure and mechanical properties of wire + arc additively manufactured 2219 aluminum alloy [J]. Journal of Materials Science & Technology, 2020, 37: 143−153.

[31] WU K Y, CAO X W, YIN T, ZENG M, LIAND Z. Metal transfer process and properties of double-wire double pulsed gas metal arc welding [J]. Journal of Manufacturing Processes, 2019, 44: 367−375.

[32] SELVI S, VISHVAKSENAN A, RAJASEKAR E. Cold metal transfer (CMT) technology — An overview [J]. Defence Technology, 2018, 14: 28−44.

[33] XU F J, LV Y H, XU B S, LIU Y X, SHU F Y, HE P. Effect of deposition strategy on the microstructure and mechanical properties of Inconel 625 superalloy fabricated by pulsed plasma arc deposition [J]. Materials & Design, 2013, 45: 446−455.

[34] LIU P W, WANG Z, XIAO Y H, HORSTEMEYER M F, CUI X Y, CHEN L. Insight into the mechanisms of columnar to equiaxed grain transition during metallic additive manufacturing [J]. Additive Manufacturing, 2019, 26: 22−29.

[35] KOU S. Welding metallurgy [M]. 2nd ed. New Jersey: John Wiley & Sons, 2002.

[36] HU Y L, LIN X, ZHANG S Y, JIANG Y M, LU X F, YANG H O, HUANG W D. Effect of solution heat treatment on the microstructure and mechanical properties of Inconel 625 superalloy fabricated by laser solid forming [J]. Journal of Alloys and Compounds, 2018, 767: 330−344.

[37] KOSTUREK R, WACHOWSKI M, ŚNIEZEK L, GLOC M. The influence of the post-weld heat treatment on the microstructure of Inconel 625/carbon steel bimetal joint obtained by explosive welding [J]. Metals, 2019, 246: 1−16.

[38] SILVA C C, de ALBUQUERQUE V H C, MINA E M, MOURA E P. TAVARES J M R S. Mechanical properties and microstructural characterization of aged nickel-based alloy 625 weld metal [J]. Metallurgical and Materials Transactions A, 2018, 49: 1653−1673.

[39] DAS A, TARAFDER S. Geometry of dimples and its correlation with mechanical properties in austenitic stainless steel [J]. Scripta Materialia, 2008, 59: 1014−1017.

热处理对电弧增材制造 Inconel 625 合金显微组织和力学性能的影响

Abolfazl SAFARZADE, Mahmood SHARIFITABAR, Mahdi SHAFIEE AFARANI

Department of Materials Engineering, Faculty of Engineering, University of Sistan and Baluchestan, P. O. Box 98135-674, Zahedan, Iran

摘　要：研究电弧增材制造 Inconel 625 合金热处理前后的显微组织和力学性能。未热处理样品的显微组织中形成枝晶镍基固溶体相、(Nb,Ti)C 碳化物、Laves 相和 δ-Ni_3Nb 二次相。固溶热处理导致 Laves 和 Ni_3Nb 相的溶解。此外，枝晶被大柱状晶取代。时效热处理导致晶界 $M_{23}C_6$ 碳化物和纳米 γ''晶的析出。未经热处理试样的硬度、屈服强度、抗拉强度和伸长率与铸态合金的接近，其断裂为穿晶韧性断裂。固溶热处理能提高合金的硬度和屈服强度，降低伸长率，但对抗拉强度影响不大。此外，时效热处理导致拉伸性能变差，断裂模式转变为穿晶韧性断裂和沿晶脆性断裂的混合模式。

关键词：镍合金；增材制造；直接能量沉积；热处理；显微组织

(Edited by Wei-ping CHEN)